MOLECULAR IMAGING AND BIOLOGY

Mol Imaging Biol (2015) 17:884–892
DOI: 10.1007/s11307-015-0849-1

Published Online: 28 April 2015

RESEARCH ARTICLE

Generation of a Four-Class Attenuation Map for MRI-Based Attenuation Correction of PET Data in the Head Area Using a Novel Combination of STE/Dixon-MRI and FCM Clustering

Parisa Khateri,[1] Hamidreza Saligheh Rad,[1,2] Amir Homayoun Jafari,[2,3,4] Anahita Fathi Kazerooni,[1,2] Afshin Akbarzadeh,[1] Mohsen Shojae Moghadam,[3,4] Arvin Aryan,[5] Pardis Ghafarian,[6,7] Mohammad Reza Ay[1,2]

[1]*Research Center for Molecular and Cellular Imaging, Tehran University of Medical Sciences, Tehran, Iran*
[2]*Department of Medical Physics and Biomedical Engineering, Tehran University of Medical Sciences, Tehran, Iran*
[3]*Research Center for Biomedical and Robotics Technology, Tehran University of Medical Sciences, Tehran, Iran*
[4]*MRI Imaging Center, Payambaran Hospital, Tehran, Iran*
[5]*Imaging Center, Imam Khomeini Hospital Complex, Tehran University of Medical Sciences, Tehran, Iran*
[6]*Chronic Respiratory Diseases Research Center, National Research Institute of Tuberculosis and Lung Diseases (NRITLD), Shahid Beheshti University of Medical Sciences, Tehran, Iran*
[7]*PET/CT and Cyclotron Center, Masih Daneshvari Hospital, Shahid Beheshti University of Medical Sciences, Tehran, Iran*

Abstract

Purpose: The aim of this study is to generate a four-class magnetic resonance imaging (MRI)-based attenuation map (μ-map) for attenuation correction of positron emission tomography (PET) data of the head area using a novel combination of short echo time (STE)/Dixon-MRI and a dedicated image segmentation method.

Procedures: MR images of the head area were acquired using STE and two-point Dixon sequences. μ-maps were derived from MRI images based on a fuzzy C-means (FCM) clustering method along with morphologic operations. Quantitative assessment was performed to evaluate generated MRI-based μ-maps compared to X-ray computed tomography (CT)-based μ-maps.

Results: The voxel-by-voxel comparison of MR-based and CT-based segmentation results yielded an average of more than 95 % for accuracy and specificity in the cortical bone, soft tissue, and air region. MRI-based μ-maps show a high correlation with those derived from CT scans (R^2>0.95).

Conclusions: Results indicate that STE/Dixon-MRI data in combination with FCM-based segmentation yields precise MR-based μ-maps for PET attenuation correction in hybrid PET/MRI systems.

Key words: PET/MRI, Attenuation correction, Attenuation map, STE pulse sequence, FCM technique

Introduction

Combination of positron emission tomography (PET) with magnetic resonance imaging has recently drawn the attention of many researchers to take advantage of highly sensitive PET data as well as the ability of MRI to yield a wide variety of anatomical and functional information [1–3]. Despite remarkable advances in PET imaging, the effect of photon attenuation still remains unsolved. Although it has been investigated that both attenuation-corrected and

Correspondence to: Mohammad Ay; *e-mail:* mohammadreza_ay@tums.ac.ir

uncorrected PET data may predict the same results for clinical application [4], generation of μ-map is still crucial in order to obtain accurate PET quantification results [5, 6].

Different approaches are used for PET attenuation correction. They can be divided into two broad classes of methods: emission-based methods and transmission-based methods. Among the first class of methods, using time-of-flight (TOF) emission data has found success in determination of attenuation factors [7, 8]. Transmission-based methods remain the most popular approach in PET imaging. In hybrid PET/X-ray computed tomography (CT) systems, the μ-map is generated by measuring the distribution of electron density across the object from CT data. Because of the limited physical space inside the PET/MRI gantry, it is not practical to insert a CT scanner in PET/MRI gantry and use these direct measurements in PET attenuation correction [3, 9]. In addition, using external CT images for generation of μ-map leads to misregistration artifact and increases patient dose. Therefore, studies have focused on using MR images to produce μ-maps in hybrid PET/MRI systems [10–12].

Magnetic resonance-based attenuation correction (MRAC) is a challenging issue, because MRI represents information about proton density and relaxation time of tissues rather than electron density. Reviewing MRI-based attenuation correction methods reveals that generation of μ-maps from MR images mainly fall into two categories: (I) template-based methods [13, 14] and (II) segmentation-based methods [10, 15, 16]. In template-based methods, the template MRI is registered to the patient MRI data. Then, the derived transformation is used to transform the template μ-map into the patient μ-map. Template-based methods are capable to yield a continuous μ-map including a range of attenuation coefficients [17]; however, they are prone to error because of patient anatomic variation, especially in sinusoidal regions of head area. In segmentation-based methods, μ-maps are directly derived from patient MRI in two steps: first, MRI images are classified into different tissues with different attenuation properties. Then, corresponding attenuation coefficients are assigned to each class [10, 15, 16].

While MRI is capable of providing high contrast between different soft tissues, it is not possible to distinguish air and bone areas using conventional MRI. The T2* relaxation time of the cortical bone tissue is very short so that bone signals decay before being detected by the receiver coils. Since there is a large difference between attenuation properties of the bone and air, it seems crucial to find a way to differentiate these classes in segmentation-based methods. It has been shown that ignoring bone regions in the μ-map leads to quantification error for PET data of up to 17 % in whole-body imaging [18] and up to 25 % in the head area [19].

Recently, a dedicated technique, named ultra-short echo time (UTE) pulse sequence, has been introduced to overcome the problem of bone detection in MRI-based PET attenuation correction [20–23]. Although combining UTE pulse sequence with the conventional counterpart is able to yield an extra bone class in the generated μ-map in 511 keV, it is not accessible in conventional MRI systems. In addition, implementation of UTE sequences is expensive and complicated, making whole-body imaging difficult and time-consuming.

The authors of this article have previously investigated that using short echo time (STE) pulse sequences could be a potential alternative for UTE pulse sequences to derive bone class in MRAC of PET data in the head region [24]. STE pulse sequences are commercially available on conventional MRI systems, and they cost less than UTE sequences. However, the ability of STE sequences in detecting bone signals is less than that of UTE sequences. To reach more accurate results of STE sequences, a segmentation method based on fuzzy C-means (FCM) clustering was proposed to distinguish bone voxels in MRI images [25].

In this study, the new STE/Dixon pulse sequence is combined with a dedicated segmentation protocol based on FCM clustering and morphologic operations to segment MRI images into four classes of the cortical bone, soft tissue, fat tissue, and air and to derive MRI-based μ-map in 511 keV. In addition, unlike previous studies conducted by the authors in this area, CT images are acquired in the present study to accurately assess the strategy and to avoid the potential bias of specialist recognition. Therefore, results are quantitatively assessed based on five datasets and using CT images to generate reference μ-maps in validation strategy.

Materials and Methods

MR Imaging

A prototype STE/MR dataset was acquired to evaluate the amount of signal-to-noise ratio in STE images and in comparison with long echo time (LTE) images from two-point Dixon pulse sequences. Measurements were acquired on a 1.5T MRI system, MAGNETOM Avanto (Siemens Medical Solutions, Erlangen, Germany). To achieve more signal and less noise, voxel size was selected to be relatively large ($1.86\times1.86\times1.63$ mm^3). In this case, minimum echo time was acquired (TE=0.8 ms). The number of excitation and repetition time (TR) was considered 5 and 8 ms, respectively, so that acquisition time was about 220 s. A corresponding Dixon pulse sequence was applied with the exact same parameters, except for the echo time to be 4.76 ms.

The ultimate MRI protocol, including a combination of STE and Dixon pulse sequences, was applied on the head regions of five volunteers to clinically evaluate the ability of the STE/Dixon technique to yield four-class attenuation maps. Two consecutive pulse sequences, STE technique based on FLASH 3D pulse sequences (echo time, 1.1 ms; repetition time, 12 ms; voxel size, $1.2\times1.2\times2$ mm^3; acquisition time, 462 s) and Dixon technique for fat and water decomposition (echo time 1, 2.38 ms; echo time 2, 4.76 ms; repetition time, 12 ms; voxel size, $1.2\times1.2\times2$ mm^3;

acquisition time, 462 s), were applied. Therefore, three MRI datasets for each volunteer were available: STE (from STE technique), in-phase, and out-of-phase images (from Dixon technique).

CT Imaging

In order to evaluate MR-based μ-maps, CT images were used to generate reference μ-map in 511 keV. Considering this fact that normal volunteers were asked to receive MR imaging, ultra-low-dose CT (ULDCT) imaging protocol (80 kVp, 10 mA, and 0.5 s rotation time) was proposed [26, 27] so that the total effective dose exposed to each person would be in the safe range according to the International Commission on Radiological Protection (ICRP) report 103 [28].

The "ImPACT CT Patient Dosimetry Calculator" (version 0.99x 20/01/06) software was used to simulate ULDCT and calculate the total effective dose imposed to each volunteer during CT imaging. The amount of total effective dose of ULDCT was compared to that of the typical CT imaging with 140 kVp, 140 mA, and 1 s rotation time. The total effective dose of ULDCT was calculated as 0.008 mSv about 0.4 % of the total effective dose of the typical CT imaging (2.1 mSv). This amount is less than 0.01 mSv that is determined by ICRP as the negligible individual dose. The proposed ULDCT protocol was approved by the Ethical Committee of Tehran University of Medical Sciences (Ethic license number 1432), and all volunteers, who were well educated about medical imaging systems, gave their written informed consent for participation. In the next step, five volunteers with available MR images experienced ULDCT scan on the CT module of Discovery 690 PET/CT scanner (GE Healthcare, Waukesha, WI).

Generation of μ-Maps from MR Images

A four-class μ-map including the cortical bone, soft tissue, fat tissue, and air regions was derived from MR images. The image analysis protocol was mainly performed by an in-house-developed software written in MATLAB (The MathWorks, Inc.). The open-source image processing software 3D slicer (http://www.slicer.org/) was also used to denoise MR images and generate manual masks for some central regions of the head containing cerebrospinal fluid (CSF).

Steps for this generation of attenuation map (u-map) from MR images are illustrated in Fig. 1, as follows:

Step 1 MR images underwent an anisotropic diffusion filtering in order to reduce the noise level while maintaining edge information of images. Water and fat images were calculated from in-phase and out-of-phase images.

Step 2 Two fuzzy clusters were obtained from each series of fat and water images. Because fat and water images represent, respectively, fat and water voxels with higher intensity, applying fuzzy clustering to fat and water images leads to clusters in which fat and water regions are more highlighted. Since in-phase images contain only signals of the soft tissue, i.e., water and fat tissues, these images were used to derive fuzzy soft clusters. Thus, the intersection of soft cluster and water cluster yielded water mask, and the intersection of soft cluster and fat cluster yielded fat mask.

Step 3 The opening morphologic filter was employed on STE images to reduce susceptibility artifact in regions of air-bone neighboring [29]. Obtained filtered images underwent FCM technique and resulted in four fuzzy clusters. One of them was identified as the air cluster in which air regions were highlighted. Air masks then emerged from air clusters. The remaining voxels that were not included in fat, water, and air masks were considered as bone voxels.

Step 4 Because the image processing method was based on voxel intensity, areas with the same intensity but different attenuation properties suffer from misclassification. This problem was observed in internal brain regions which were misclassified as bone. Since misclassified brain tissues were far away from bone regions, they could be accurately distinguished from bone class. Therefore, a manual mask using 3D slicer software was generated to exclude the brain tissue from bone mask.

Step 5 A closing morphologic operation was applied on segmented bone regions in order to adjoin the area of discontinuities [29], followed by a dilating morphologic operation to bold bone regions, because bone regions are depicted smaller than their actual size in MR images.

Step 6 After segmentation of MRI images into four classes of bone, water, fat, and air, μ-maps were generated by assigning corresponding attenuation coefficients in 511 keV to each class. Tissue attenuation coefficients were calculated using tissue mass attenuation coefficients and average tissue densities obtained from the International Commission on Radiation Units and Measurements (ICRU) 44 report [30]. Then, μ-maps were down-sampled and smoothed by a Gaussian filter with 5 mm full width at half maximum to be matched with the resolution of PET images.

Generation of μ-Maps from CT Images

In the first step, the CT images were registered to the MRI images in order to minimize the misregistration between generated μ-maps from CT and MRI images. Thereafter, the CT images were segmented into three classes of bone, soft tissue, and air regions using a simple thresholding method. The thresholds were set as 550 and −350 HU by plotting CT image histogram. After segmentation, corresponding attenuation coefficients in 511 keV (calculated based on ICRU 44 report) were assigned to regions with different attenuation properties. Then, CT-based μ-maps were derived by down-sampling and

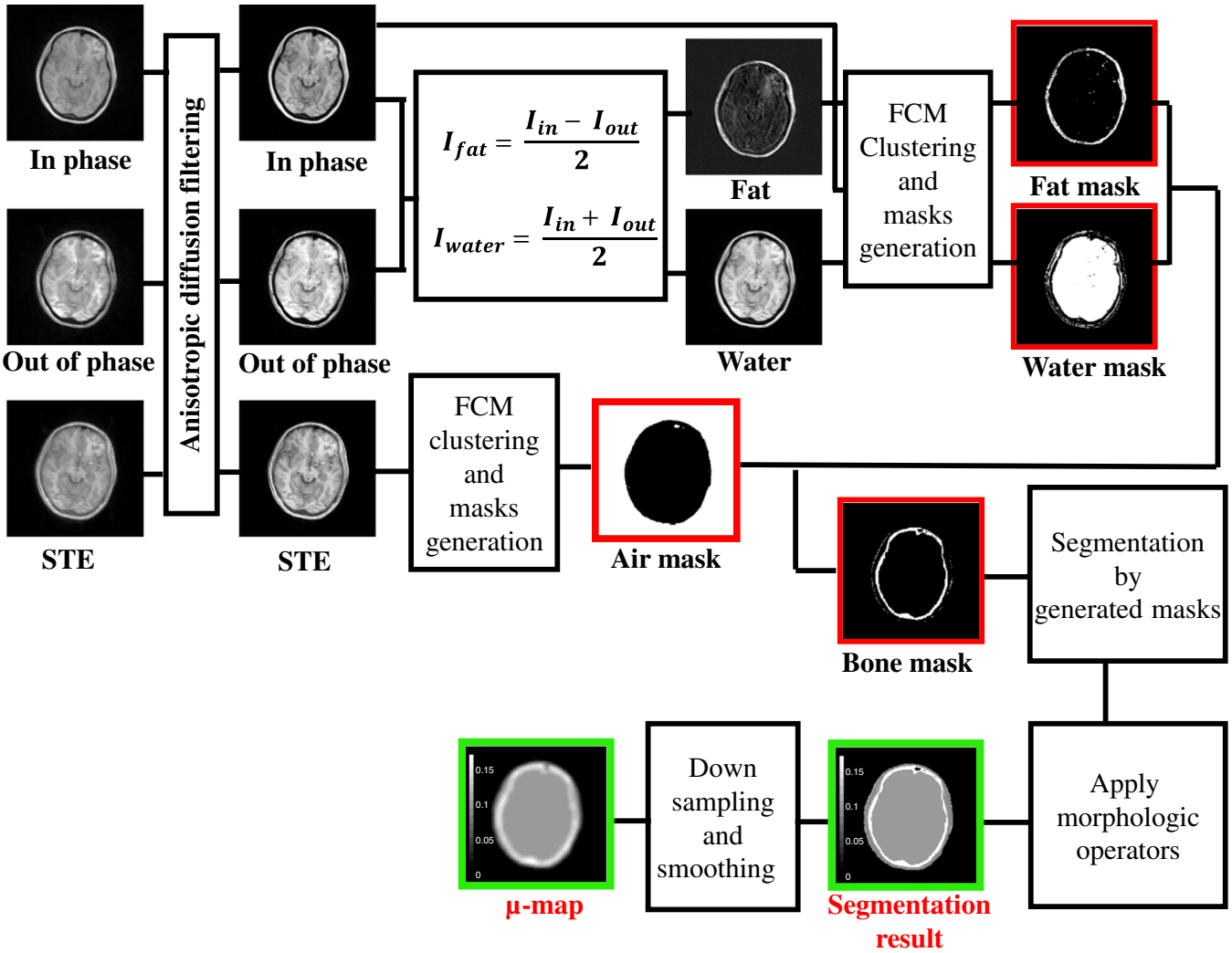

Fig. 1 Generation of MR-based μ-maps by manipulating STE and Dixon images.

smoothing (using Gaussian filter with 5 mm full width at half maximum) the segmentation results.

MRI and CT Registration

CT images were registered to MR images using FSL Linear Image Registration Toolbox (http://fsl.fmrib.ox.ac.uk/fsl/fslwiki/FLIRT). A 3D registration was performed using affine transformation model and trilinear interpolation technique. The cost function was selected to be normalized mutual information (NMI), which is suitable for multimodal image registration. Prior to registration, a brain mask was created for CT images using "Chan-Vese" active contour segmentation method to eliminate unnecessary information from the head area, such as background details with similar intensities to those of the brain tissue, and to achieve better alignment with MR images. The active contour snake function evolves over several iterations to capture the border of the head and to separate it from the surrounding area. The region inside the captured border was used as a mask which consequently was multiplied by the corresponding CT image.

Evaluation Strategy

SNR Measurement

Signal-to-noise ratio (SNR) was calculated in six different regions of interest (ROIs) of bone regions selected by an expert radiologist. To calculate SNR, average signal of each ROI was divided by the average noise of the near background area. For a reasonable comparison, the same calculation was performed in adjacent soft tissue ROIs. These measurements were performed on two STE and LTE datasets, as depicted in Fig. 2. Then, SNR of the bone was divided to SNR of the adjacent soft tissue. This ratio was obtained to consider soft tissue SNR as reference, while comparing the bone SNR of the two STE and LTE datasets.

Quantitative Assessment

Fifteen slices of each dataset with a distance of about three slices from each other were considered to be analyzed in the evaluation strategy. To assess segmentation method and to quantify the

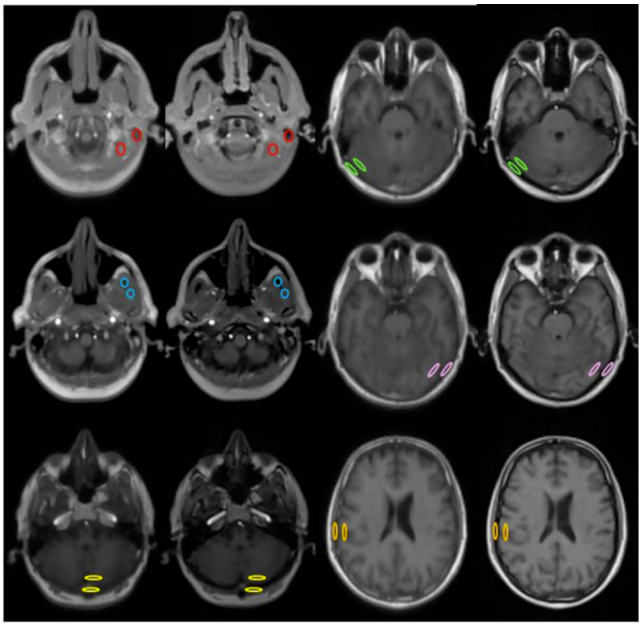

Fig. 2 STE and corresponding LTE images. Six pairs of ROIs of the bone and soft tissue were selected to evaluate the bone SNR.

similarity between CT-based and MR-based segmentation results, the values of sensitivity, specificity, and accuracy were calculated performing a voxel-by-voxel comparison between segmentation results, and as follows:

$$\text{Sensitivity} = \frac{\text{TP}}{(\text{FN} + \text{TP})}$$

$$\text{Specificity} = \frac{\text{TN}}{(\text{FP} + \text{TN})}$$

$$\text{Accuracy} = \frac{(\text{TP} + \text{TN})}{(\text{FN} + \text{TP} + \text{FP} + \text{TN})}$$

CT-based segmentation results were considered as reference images to calculate values of true positive (TP), false positive (FP), true negative (TN), and false negative (FN). These three values were calculated for three classes of the soft tissue (integration of fat and water tissue classes), cortical bone, and air. It should be noted that ULDCT images were not considered as reference to assess fat-water decomposition, since two-point Dixon sequence is a standard method to differentiate between fat and water.

The overall accuracy of STE/Dixon-based segmentation results was calculated by performing a voxel-by-voxel comparison to the segmented CT-based segmentation results. For each class on the CT-based segmentation results, the percentage of voxels that was assigned to the correct and incorrect classes was calculated.

Correlation Plot

To assess the similarity (in the form of correlation) between MR-based and CT-based μ-maps, joint histogram was plotted. The histograms of μ-maps of all slices for each CT and MR dataset were integrated in two arrays to plot a total joint histogram and to calculate average correlation coefficient between MR-based and CT-based μ-maps. The attenuation correction factor (ACF) sinograms were generated by forward projection of generated μ-maps followed by an exponential transform. Then, the correlation between MR-based and CT-based ACF sinograms was measured.

Results

STE/Dixon-MRI and CT examinations were performed in all participant volunteers successfully. Prototype MRI dataset with larger voxel size undergone the SNR measurement. Table 1 illustrates SNR measurements of cortical bone and soft regions for both STE and LTE images.

Exemplary slices for areas of different complexities of acquired MR images including STE, fat, and water images, as well as the corresponding registered CT images, are illustrated in Fig. 3.

Segmentation results, corresponding μ-maps, and the difference between MR and CT results for the same slices in Fig. 3 are shown in Figs. 4 and 5.

The quantitative assessment for the three classes of the cortical bone, soft tissue, and air region are summarized in Table 2. Average values of accuracy (Ac.), specificity (Sp.), and sensitivity (Sen.) across five datasets were calculated in comparison with CT data. Values of accuracy and specificity were more than 95 % for all three classes; however, the average value of sensitivity was calculated 75 % for the cortical bone and more than 90 % for other classes.

An overall evaluation of the classification accuracy was performed to investigate the true fraction of classified voxels compared with CT images. For each class of the cortical bone, soft tissue, and air region, the fraction of voxels that were assigned to the true or false classes was determined. The average of these fractions is illustrated in Fig. 6.

In order to evaluate μ-maps and their effect on reconstruction process of PET imaging, the correlation between MR and CT μ-maps and ACF sinograms were calculated. The correlation coefficient for both μ-maps and ACF sinograms of the less complex sample slice (as shown in Fig. 3) was calculated as 0.99. The more complicated slices yielded the correlation coefficients of 0.98 and 0.96 for μ-maps and ACF sinograms, respectively. As it was expected, results show more similarity in data with less complexity.

To achieve an overall view, all 15 MRI-based and CT-based μ-maps of each dataset were integrated in two arrays, and the correlation between them was calculated. The same assessment was conducted for ACF sinograms (Fig. 7).

Table 1. Quantitative assessment results for bone segmentation considering radiologist bone extraction as reference

Tissue class		Average SNR	$\frac{\text{SNR}_{\text{bone}}}{\text{SNR}_{\text{soft tissue}}}$
STE	Bone	99.0	0.6
	Soft tissue	163.7	
LTE	Bone	7.1	0.1
	Soft tissue	71.3	

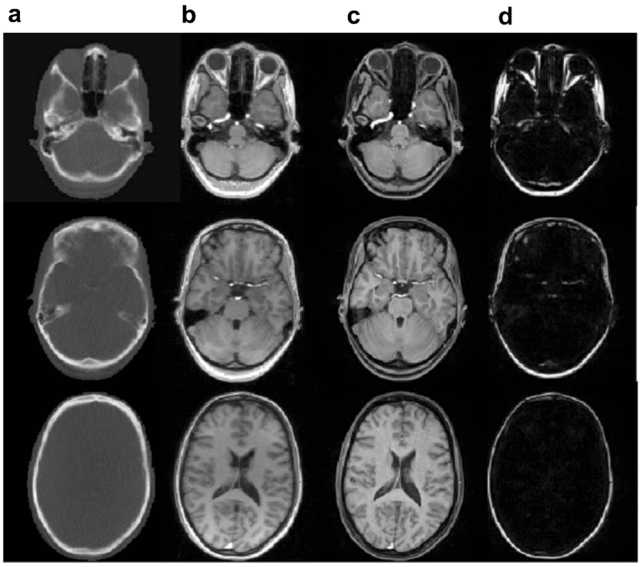

Fig. 3 **a** CT images and corresponding MRI data including **b** STE, **c** water, and **d** fat images are illustrated. Example slices of varying complexities are shown.

Results yielded an overall correlation coefficient of 0.98 and 0.97 for integrated μ-maps and ACF sinograms over 15 slices.

Discussion

This study was motivated by proposing STE pulse sequence in bone signal detection from MRI data to derive the cortical bone as a separate class in PET attenuation correction. SNR ratio of bone to soft tissue was calculated to obtain a measure which indicates the STE pulse sequence ability to detect bone signal relative to the LTE pulse sequence. This ratio increases six times for STE images relative to LTE images which shows an increase in detection of bone signal in STE sequences.

In this study, the use of STE/MRI along with a robust image analysis method for generation of PET μ-maps was evaluated on five datasets of normal volunteers in comparison with CT images. Results indicate a good agreement between CT- and MR-based μ-maps. Different images between CT and MRI segmentation results, as well as the μ-maps, represented that ethmoid sinuses are the most error-prone regions of the head area. The largest difference was observed about 0.05 cm^{-1} in the paranasal area. This amount could be attributed to the MRI susceptibility artifact. Although in this study morphologic operations were applied on MRI images to reduce susceptibility error, using atlas-based susceptibility artifact correction methods could be a potential solution to prevent error in the sinus area [31].

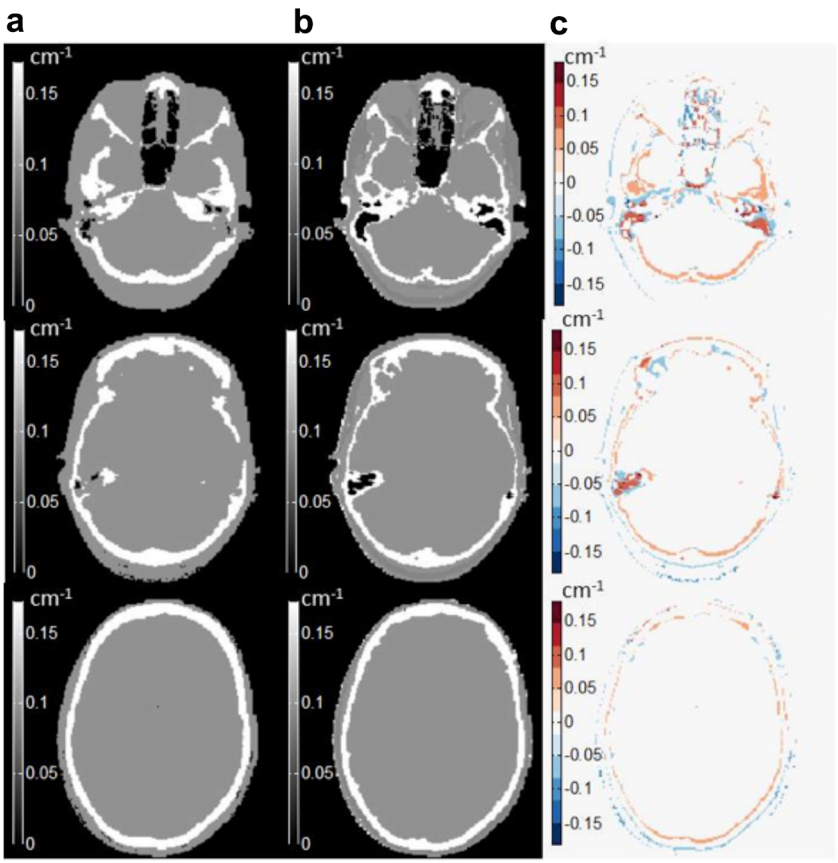

Fig. 4 Segmentation results derived from **a** CT images, **b** MRI and **c** the difference between segmentation results for the same slices of Fig. 3 are illustrated.

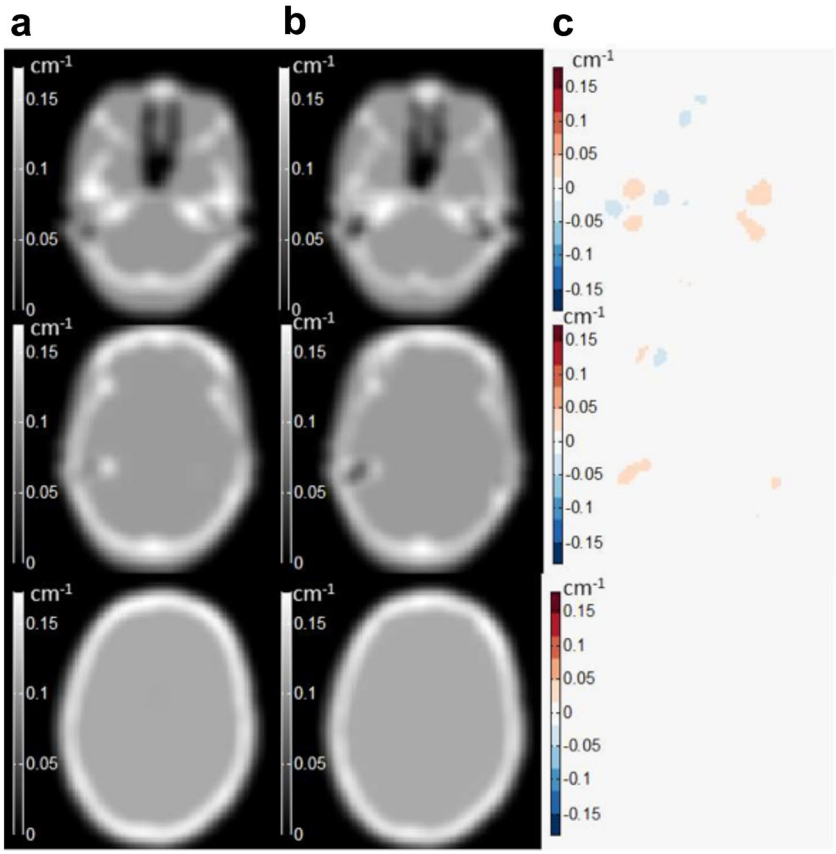

Fig. 5 μ-maps derived from **a** CT **b** and MRI images and **c** the difference between μ-maps for the same slices of Fig. 3 are illustrated.

A previous study conducted by the authors of this study [25] used radiologist specialists to predict bone class as reference in the validation strategy. In this study, CT images were acquired to accurately go through the assessment strategy and to avoid the potential bias of specialist recognition. CT images paved the way to classify the head area into classes of the cortical bone, soft tissue, and air and to evaluate the ability of STE/MRI to provide accurate μ-maps in 511 keV.

Visual comparison of results indicates that generation of μ-maps from segmentation results, i.e., down-sampling and smoothing, increases similarity between MR and CT results, so that for the area of low complexity, the different images show no difference between MR and CT μ-maps. It is also observed in different images that areas of more complexity represent more error in the sinusoidal region in comparison with CT results.

Quantification assessment yielded an average value of more than 95 % for specificity and accuracy for all classes. Therefore, the current method is capable of classifying different tissue types in PET μ-maps. These values confirmed previously published results [25] and showed that a combination of STE pulse sequence with a robust image processing method based on the FCM technique can be a potential alternative for UTE/MRI in PET attenuation correction.

The amount of sensitivity for the bone class was reported to be about 75 %. At first glance, it may seem that susceptibility artifact in the vicinity of bone tissue causes this area to be more error prone rather than other classes. This is rarely true, and the main reason is the small fraction of bone voxels in relation to other classes in the investigated area. In other words, since the number of bone voxels is very few, small variations in this number cause big changes in the sensitivity.

Table 2. Quantitative assessment results for three classes of cortical bone, soft tissue, and air

Segmented class	Cortical bone			Soft tissue			Air		
Parameter	Ac.	Sp.	Sen.	Ac.	Sp.	Sen.	Ac.	Sp.	Sen.
Average value	0.96	0.97	0.75	0.95	0.97	0.95	0.96	0.98	0.92

Ac. Accuracy, *Sp*. Specificity, *Sen*. Sensitivity

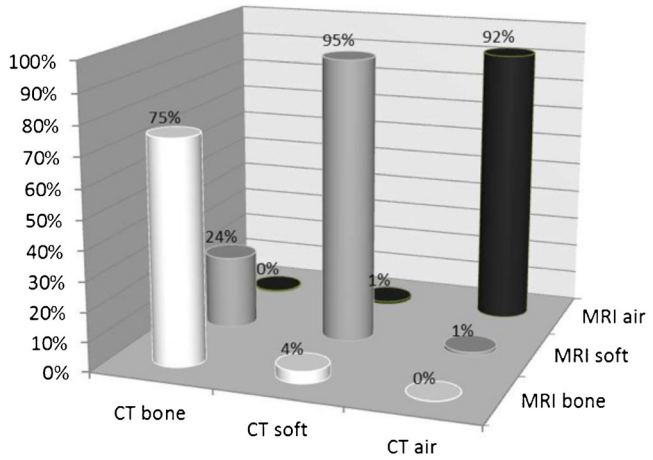

Fig. 6 An overall evaluation to investigate the fraction of true and false classified voxels is shown.

The segmentation method of this study was based on FCM technique in which voxel intensity is considered to identify different classes. It would be useful to use region-based segmentation methods along with intensity-based methods like FCM to avoid manual intervention and to implement automated classification in the area with the same intensity but different attenuation properties. Using CT images as reference was subject to misregistration error, because CT volumes were acquired on a separate CT system located far from the MRI system. Thus, motion artifact and different field of views potentially imposed a small bias in image registration.

The correlation coefficient between MRI-based and CT-based μ-maps indicates a high amount of about $R^2>0.95$ which shows a good agreement between results. To compensate the lack of access to PET images, ACF sinograms were also calculated from μ-maps to assess the impact of generated μ-maps on PET reconstruction. Likewise, results reported a high correlation between ACF sinograms showing that the impact of attenuation correction using STE/MRI and CT images would be very similar. It would be interesting to evaluate the impact of the proposed MRI-based attenuation correction on PET quantification data by simultaneous PET/MRI systems.

Visual assessment of segmentation results and generated μ-maps showed that there is still misclassification in complicated regions like ethmoid sinuses; however, recent studies that investigated the impact of UTE/MRI on PET attenuation correction also showed the same misclassification in complex area where air and bone are adjacent or in CSF regions [20, 22].

Based on the voxel-wise comparison between the segmentation results of MRI and CT images, our method was able to classify air from the tissue with the overall accuracy of about 92 %. In other words, 92 % of air voxels were correctly classified (Fig. 6). The highest misclassification was observed between bone and soft tissue; 24 % of bone voxels were misclassified as soft tissue, and about 4 % of soft tissue voxels were assigned as cortical bone. A recent study by Vincent Keereman investigating the UTE-based attenuation correction [32] reported an incorrect classification of 25 % for bone voxels as soft tissue and 20 % for soft tissue voxels as bone.

Conclusion

The current STE-MRI-based attenuation correction introduces an innovative approach for attenuation correction of PET data in hybrid PET/MRI systems. As a consequence, implementation of the proposed approach can be a good alternative for UTE-based MRAC in attenuation of PET data for conventional MRI systems. The validation strategy based on a comparison of the proposed MRAC method to CTAC as reference represents high similarity between two datasets.

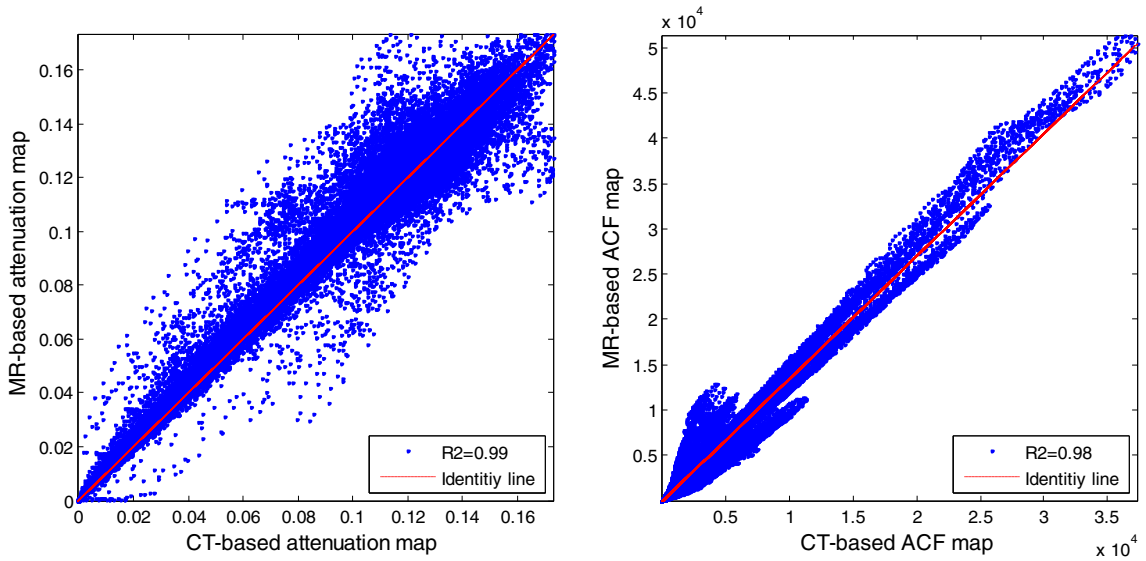

Fig. 7 Joint histograms of integrated μ-maps and integrated ACF sinograms.

Acknowledgments. This work was supported by the Tehran University of Medical Sciences under grant no. 25095.

Conflict of Interest. The authors declare that they have no conflict of interest.

References

1. Heiss W-D (2009) The potential of PET/MR for brain imaging. Eur J Nucl Med 36(1):105–112
2. Pichler BJ, Kolb A, Nägele T, Schlemmer H-P (2010) PET/MRI: paving the way for the next generation of clinical multimodality imaging applications. J Nucl Med 51(3):333–336
3. Zaidi H, Del Guerra A (2011) An outlook on future design of hybrid PET/MRI systems. Med Phys 38:5667
4. Joshi U, Raijmakers PG, Riphagen II et al (2007) Attenuation-corrected vs. nonattenuation-corrected 2-deoxy-2-[f-18] fluoro-d-glucose-positron emission tomography in oncology, a systematic review. Mol Imaging Biol 9(3):99–105
5. Turkington TG (2000) Attenuation correction in hybrid positron emission tomography [abstract]. Semin Nucl Med Elsevier 30:255–267
6. Akbarzadeh A, Ay M, Ahmadian A et al (2013) MRI-guided attenuation correction in whole-body PET/MR: assessment of the effect of bone attenuation. Ann Nucl Med 27(2):152–62
7. Rezaei A, Defrise M, Bal G et al (2012) Simultaneous reconstruction of activity and attenuation in time-of-flight pet. IEEE Trans Med Imaging 31(12):2224–2233
8. Rezaei A, Defrise M, Nuyts J (2014) Ml-reconstruction for tof-pet with simultaneous estimation of the attenuation factors. IEEE Trans Med Imaging 33(7):1563–1572
9. Keereman V, Mollet P, Berker Y et al (2013) Challenges and current methods for attenuation correction in PET/MR. Magn Reson Mater Phys Biol Med 26(1):81–98
10. Zaidi H, Montandon M-L, Slosman DO (2003) Magnetic resonance imaging-guided attenuation and scatter corrections in three-dimensional brain positron emission tomography. Med Phys 30:937
11. Fei B, Yang X, Wang H (2009) An MRI-based attenuation correction method for combined PET/MRI applications [abstract]. SPIE Med Imaging Int Soc Opt Photon 27:7262
12. Hofmann M, Steinke F, Scheel V et al (2007) MR-based PET attenuation correction–method and validation [abstract]. IEEE NSS-MIC 2007 49:1875–1883
13. Hofmann M, Steinke F, Scheel V et al (2008) MRI-based attenuation correction for PET/MRI: a novel approach combining pattern recognition and atlas registration. J Nucl Med 49(11):1875–1883
14. Malone IB, Ansorge RE, Williams GB et al (2011) Attenuation correction methods suitable for brain imaging with a PET/MRI scanner: a comparison of tissue atlas and template attenuation map approaches. J Nucl Med 52(7):1142–1149
15. Martinez-Möller A, Souvatzoglou M, Delso G et al (2009) Tissue classification as a potential approach for attenuation correction in whole-body PET/MRI: evaluation with PET/CT data. J Nucl Med 50(4):520–526
16. Schulz V, Torres-Espallardo I, Renisch S et al (2011) Automatic, three-segment, MR-based attenuation correction for whole-body PET/MRI data. Eur J Nucl Med 38(1):138–152
17. Navalpakkam BK, Braun H, Kuwert T, Quick HH (2013) Magnetic resonance–based attenuation correction for pet/mr hybrid imaging using continuous valued attenuation maps. Invest Radiol 48(5):323–332
18. Keereman V, Van Holen R, Mollet P, Vandenberghe S (2011) The effect of errors in segmented attenuation maps on PET quantification. Med Phys 38(11):6010–6019
19. Andersen FL, Ladefoged CN, Beyer T et al (2014) Combined PET/MR imaging in neurology: MR-based attenuation correction implies a strong spatial bias when ignoring bone. Neuroimage 84:206–216
20. Catana C, van der Kouwe A, Benner T et al (2010) Toward implementing an MRI-based pet attenuation-correction method for neurologic studies on the MR-PET brain prototype. J Nucl Med 51(9):1431–1438
21. Keereman V, Fierens Y, Broux T et al (2010) MRI-based attenuation correction for PET/MRI using ultrashort echo time sequences. J Nucl Med 51(5):812–818
22. Berker Y, Franke J, Salomon A et al (2012) Mri-based attenuation correction for hybrid PET/MRI systems: a 4-class tissue segmentation technique using a combined ultrashort-echo-time/Dixon MRI sequence. J Nucl Med 53(5):796–804
23. Buerger C, Aitken A, Tsoumpas C et al (2011) Investigation of 4D PET attenuation correction using ultra-short echo time mr [abstract]. IEEE NSS-MIC 2011, IEEE 3558–3561
24. Khateri P, Rad HS, Fathi A, Ay MR (2012) Generation of attenuation map for MR-based attenuation correction of PET data in the head area employing 3D short echo time MR imaging. Nucl Instrum Meth Phys Res Sect A 702: 133–136
25. Khateri P, Rad HS, Jafari AH, Ay MR (2014) A novel segmentation approach for implementation of MRAC in head PET/MRI employing short-TE MRI and 2-point Dixon method in a fuzzy c-means framework. Nucl Instrum Methods Phys Res, Sect A 734:171–174
26. Fahey FH, Palmer MR, Strauss KJ et al (2007) Dosimetry and adequacy of CT-based attenuation correction for pediatric PET: phantom study 1. Radiology 243(1):96–104
27. Xia T, Alessio AM, De Man B et al (2012) Ultra-low dose CT attenuation correction for PET/CT. Phys Med Biol 57(2):309
28. Valentin J (2007) The 2007 recommendations of the international commission on radiological protection: user's edition. Int Comm Radiol Prot 37: 2-4
29. Serra J (1982) Image analysis and mathematical morphology. Academic, London
30. ICRU (1989) International commission on radiation units and measurements, report no. 44
31. Bezrukov I, Schmidt H, Mantlik F et al (2013) MR-based attenuation correction methods for improved pet quantification in lesions within bone and susceptibility artifact regions. J Nucl Med 54(10):1768–1774
32. Keereman V (2011) MRI-based attenuation correction for emission tomography [Thesis]